Editors' Suggestion

Interlayer Electron-Hole Friction in Tunable Twisted Bilayer Graphene Semimetal

D. A. Bandurin,[1,*] A. Principi,[2,†] I. Y. Phinney,[3] T. Taniguchi,[4] K. Watanabe,[5] and P. Jarillo-Herrero[3,‡]

[1]Department of Materials Science and Engineering, National University of Singapore, 117575 Singapore
[2]School of Physics and Astronomy, University of Manchester, Manchester M13 9PL, United Kingdom
[3]Massachusetts Institute of Technology, Cambridge, Massachusetts 02139, USA
[4]International Center for Materials Nanoarchitectonics, National Institute of Material Science, Tsukuba 305-0044, Japan
[5]Research Center for Functional Materials, National Institute of Material Science, Tsukuba 305-0044, Japan

(Received 4 June 2022; revised 22 August 2022; accepted 21 October 2022; published 10 November 2022)

Charge-neutral conducting systems represent a class of materials with unusual properties governed by electron-hole (e-h) interactions. Depending on the quasiparticle statistics, band structure, and device geometry these semimetallic phases of matter can feature unconventional responses to external fields that often defy simple interpretations in terms of single-particle physics. Here we show that small-angle twisted bilayer graphene (SA TBG) offers a highly tunable system in which to explore interactions-limited electron conduction. By employing a dual-gated device architecture we tune our devices from a nondegenerate charge-neutral Dirac fluid to a compensated two-component e-h Fermi liquid where spatially separated electrons and holes experience strong mutual friction. This friction is revealed through the T^2 resistivity that accurately follows the e-h drag theory we develop. Our results provide a textbook illustration of a smooth transition between different interaction-limited transport regimes and clarify the conduction mechanisms in charge-neutral SA TBG.

DOI: 10.1103/PhysRevLett.129.206802

Low-dimensional electron-hole (e-h) systems have recently emerged as an important platform in which to explore many-body quantum phenomena. In such systems, strong Coulomb interaction among electrons and holes can give rise to a plethora of exotic quantum phases whose inventory encompasses superfluids [1,2], correlated density wave states [3,4], excitonic insulators [5,6], and Wigner crystals [4,7], to name a few. Particularly interesting interacting e-h mixtures are hosted by graphene and its bilayer. Graphene-based devices enabled the discovery of novel nontrivial effects governed by e-h interactions: from the Wiedemann-Franz law violation [8] and the anomalous Coulomb drag [9–14] to the quantum critical conductivity [15–17] and giant thermal diffusivity [18]. Central in these effects is the dominance of momentum-conserving e-h collisions over other momentum-relaxing scattering processes brought about by graphene's weak electron-phonon coupling and low disorder [19]. As a result, the behavior of graphene's e-h plasma at elevated temperatures T, often referred to as Dirac fluid, resembles that of interacting relativistic fluids governed by the laws of (relativistic) hydrodynamics [8,19–22]. Since hydrodynamics offers a natural framework by which to probe the long-wavelength behavior of strongly interacting fluids, experiments on model platforms, such as graphene, can give insights for observations in more exotic quantum phases of matter [23,24], substantiating the interest in the field.

So far, the hydrodynamic behavior of interacting e-h plasmas in mono- and bilayer graphene (MLG and BLG respectively) was explored deep in the nondegenerate limit ($E_F \ll k_B T$, where E_F is the Fermi energy, k_B is the Boltzmann constant) [8,18,25–27]. The ambipolar hydrodynamics in the degenerate regime ($E_F \gg k_B T$) as well as its genesis from the Boltzmann phase have at present remained inaccessible. This inaccessibility stems from the fact that the conduction and valence band extrema in MLG and BLG coincide in momentum space and thus the e-h system can only be realized through the smearing of the charge neutrality point (NP); adding more carriers into the system converts the neutral Dirac fluid into a unipolar Fermi liquid (FL) [19]. In this Letter, we introduce biased SA TBG as a convenient system in which to explore a smooth crossover between the Dirac fluid regime and the regime of degenerate e-h FL. In the latter case, we demonstrate that frequent momentum-conserving (yet velocity-relaxing) e-h collisions are the limiting factor for the SA TBG conductivity.

We start by exploring the single-particle band structure of SA TBG which is folded within a reduced Brillouin zone (BZ) [28] due to superlattice periodicity [Figs. 1(a) and 1(b)]. At small energies, it resembles that of MLG but is characterized by a decreased Fermi velocity v_F. Like the BZ of MLG, the reduced BZ of SA TBG is hexagonal and comprises two minivalleys located at the k_m and k'_m high symmetry points. These coincide with the K points of the two decoupled graphene sheets [28]. A prominent feature of the SA TBG is that, away from the magic angle ($\theta > 1.1°$), one can selectively populate its minivalleys

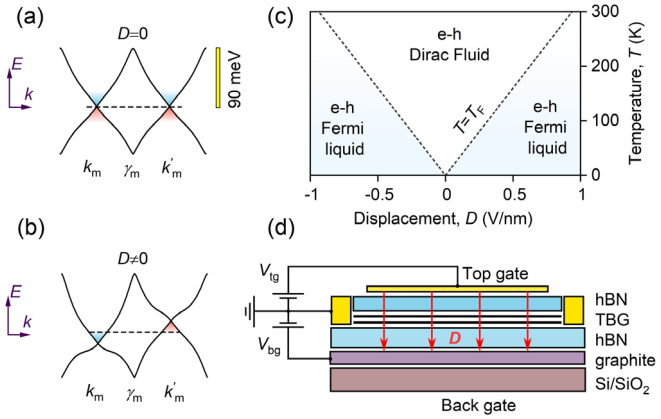

FIG. 1. Biased SA TBG. (a),(b) Single-particle band structure for SA TBG [34,35]. At low energies, two Dirac cones are formed in the vicinity of the k_m and k'_m points (a); when $D \neq 0$, the cones are shifted with respect to each other (b). The horizontal dashed lines represent the Fermi level in the neutral SA TBG. (c) Phase diagram for the charge-neutral e-h mixture in SA TBG mapped onto a T-D plane. Dashed lines: the dependence of T_F in each minivalley on D for $n = 0$. (d) Schematic of the dual-gated encapsulated SA TBG device.

with charge carriers of opposite types using a perpendicular displacement field D [(Fig. 1(b)] [3,29–33]. Electrostatic calculations [30] for $D = 1$ V/nm, reveal that such a strong D, readily achievable in experiments, can result in the formation of relatively large electron and hole Fermi surfaces in the k_m and k'_m minivalleys, respectively. Quantitatively, in each minivalley, the Fermi temperature T_F exceeds room T, as in normal FLs [Fig. 1(c) dashed line]. On the contrary, charge-neutral SA TBG at $D = 0$ is half filled up to the Dirac point where the Fermi surfaces shrink to two points and where the Dirac fluid emerges at elevated T [8,19]. This tunability enables the exploration of e-h plasma at the crossover between the Dirac fluid and FL regimes in standard transport experiments as we schematically illustrate on the D-T diagram in Fig. 1(c).

To probe such a crossover, we fabricated a dual-gated multiterminal Hall bar made out of $\theta \approx 1.65°$ SA TBG encapsulated between two relatively thin (< 100 nm thick) slabs of hexagonal boron nitride (h-BN). At this angle, the SA TBG is characterized by enhanced interaction strength and a reduced v_F, but is far enough from the magic angle (1.1°) that it allows for appreciable interlayer polarization [3,31]. The device was produced by a combination of tear-and-stack [36–39] and hot release [40] methods, and had a width of 2 μm [inset of Fig. 2(b)] (Supplemental Material [41]). The dual-gated configuration [Fig. 1(d)] allowed us to control the interlayer displacement $D/\epsilon_0 = (C_{BG}V_{BG} - C_{TG}V_{TG})/2$, and the total externally induced carrier density, $n = (C_{BG}V_{BG} + C_{TG}V_{TG})/e$, where $C_{TG,BG}$ are the top and bottom gate capacitance per unit area, ϵ_0 is the dielectric permittivity of vacuum, and e is the electron charge.

Figure 2(a) shows an example of the longitudinal resistivity ρ_{xx} dependence on V_{BG} and V_{TG} in the form of a 2D map, measured in our SA TBG and reveals its characteristic behavior. Namely, the map consists of three diagonal lines: central, which denotes the global neutrality, and two side diagonals, labeled as BI (band insulator), that reflect the full filling of the first miniband where the single-particle band insulator emerges [37,38,43]. The BI lines allow for an accurate determination of the twist angle [37,38,43]. Below, we will only focus on the region in the vicinity of the global neutrality and away from the BI and van Hove singularities.

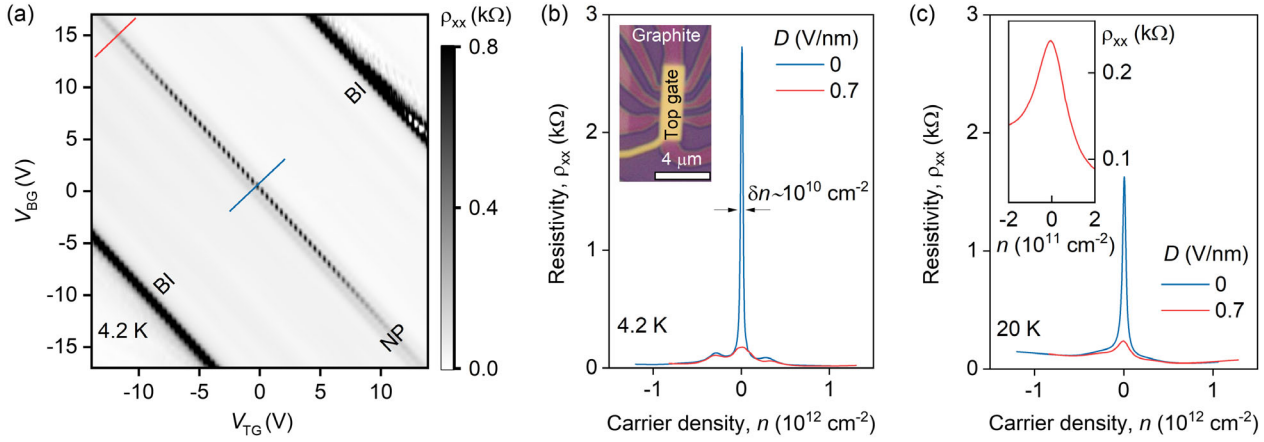

FIG. 2. Effect of displacement on the transport properties of the SA TBG. (a) ρ_{xx} as a function of V_{BG} and V_{TG} measured in the 1.65° SA TBG device. Blue and red lines correspond to the (V_{TG}, V_{BG}) points where $D = 0$ and $D = 0.7$ V/nm respectively. (b) $\rho_{xx}(n)$ traces for $D = 0$ and $D = 0.7$ V/nm measured at $T = 4.2$ K. Inset: Optical photograph of an encapsulated SA TBG device. We attribute low-T bulges in the resistivity at $|n| \simeq 10^{11}$ cm^{-2} to the manifestation of composite supermoiré lattices with a very long wavelength that could form due to unintentional and coarse alignment of graphene sheets with both boron nitride flakes [42]. (c) Same as (b) but for $T = 20$ K. Inset: enlarged region of the NP vicinity for $D = 0.7$ V/nm.

Figure 2(b) shows the $\rho_{xx}(n)$ dependence of our SA TBG device measured at $D = 0$ and $T = 4.2$ K [the curve is measured along the blue trace in the map from Fig. 2(a)]. At $D = 0$, $\rho_{xx}(n)$ exhibits a sharp peak and reaches 2.7 kΩ at $n = 0$, a standard behavior for SA TBG devices. The peak width is only $\delta n \simeq \times 10^{10}$ cm^{-2}, which indicates low charge inhomogeneity provided by the graphite gate [44]. Upon doping, $\rho_{xx}(n)$ rapidly decreases and already at 10^{12} cm^{-2} drops to 30 Ω which translates to the 1.7 μm mean free path, obtained from the standard Drude model. At liquid helium T, we also observed negative transfer resistance measured in the bend geometry (Supplemental Material [41]), indicative of the micrometer-scale ballistic transport [45,46]. These observations highlight an exceptional quality of our encapsulated SA TBG device critical for further exploration of interaction-dominated transport at elevated T.

With the application of D, the transport properties of neutral SA TBG change drastically [Fig. 2(b), red curve]. ρ_{xx} at the NP drops by more than 1 order of magnitude and becomes comparable to that of doped SA TBG (cf ρ_{xx} at 10^{12} cm^{-2}). This qualitative behavior remains unchanged upon increasing T [Fig. 2(c)]. Namely, at $T = 20$ K the NP resistivities measured at zero and finite D differ by more than 1 order of magnitude. The drop of ρ_{xx} with increasing D signals parallel conduction of two minivalleys when each of them is doped away from their NPs.

Figures 3(a) and 3(b) show $\rho_{xx}(n)$ dependencies for varying T for the case of zero (a) and finite (b) D respectively. Away from the NP ($n = 0$), ρ_{xx} grows with

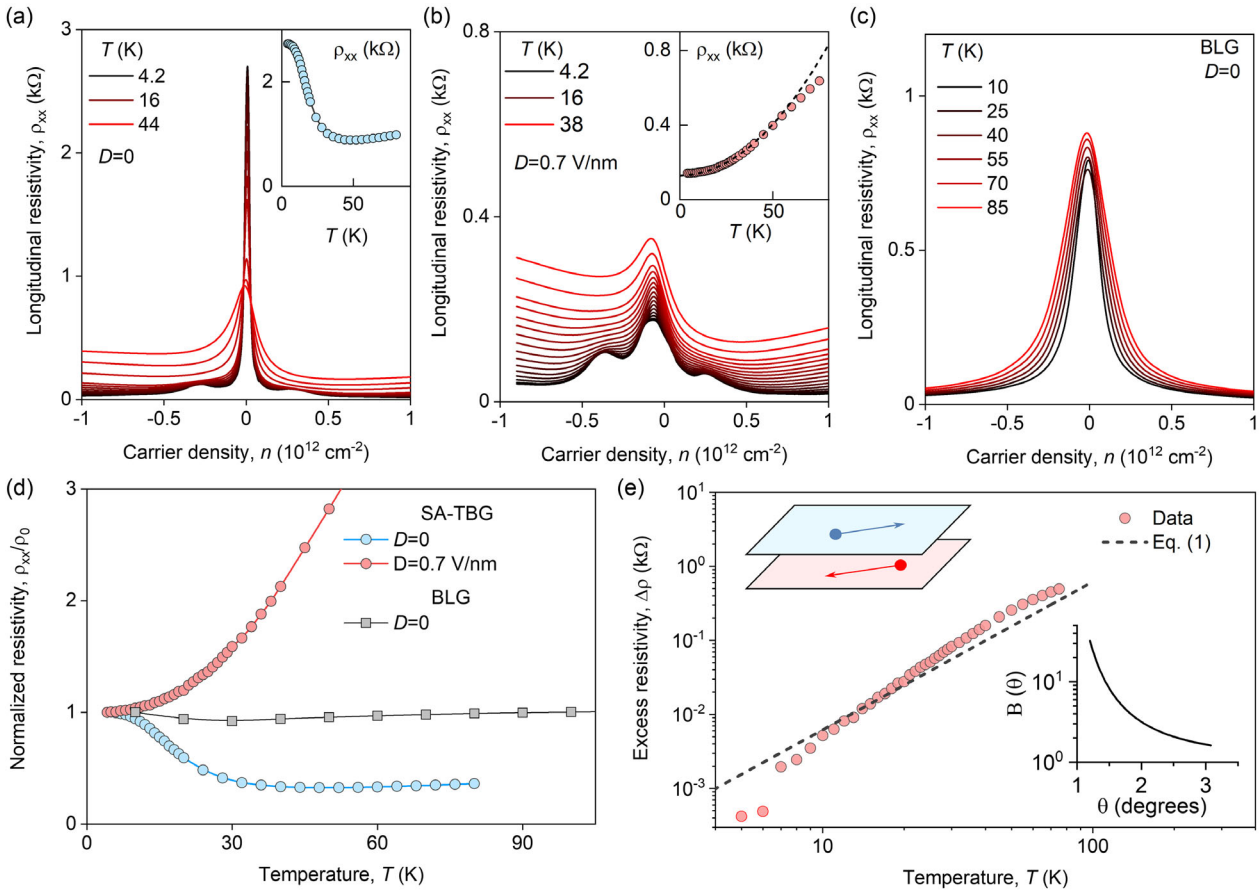

FIG. 3. Temperature dependence of the SA TBG resistivity. (a) $\rho_{xx}(n)$ for different T for the case of $D = 0$. Inset: $\rho_{xx}(T)$ at the NP and $D = 0$. (b) Same as (a) but for $D = 0.7$ V/nm. Inset: $\rho_{xx}(T)$ at the compensation point ($n = 0$) and $D = 0.7$ V/nm. Dashed line: guide for the eye that represents the $a + bT^2$ dependence. The deviation from the T^2 scaling can be attributed to the thermal smearing of the distribution function that leads to the exit of the SA TBG e-h system from the degenerate state: at $n = 1.3 \times 10^{11}$ cm^{-2}, the Fermi temperature of the 1.65° SA TBG is of the order of 220K. (c) $\rho_{xx}(n)$ for BLG at $D = 0$. (d) Resistivity as a function of T for the charge-neutral SA TBG at $D = 0$ (blue) and $D = 0.7$ V/nm (red) and for BLG at $D = 0$ (gray). The data are normalized to the lowest-T value of $\rho_{xx}(n)$: 4.2 K for SA TBG and 10 K for BLG. (e) $\Delta\rho = \rho_{xx}(T) - \rho_{xx}(4.2\text{ K})$ as a function of T measured at $D = 0.7$ V/nm and $n = 0$ (symbols). Note, $\Delta\rho(T)$ exhibits somewhat faster T dependence at $T < 15$ K. This apparent behavior is spurious and is related to the subtraction operation of the $\rho_0 = \rho_{xx}(4.2\text{ K})$ from the experimental dataset rather than ρ_{xx} at $T \to 0$. Solid line: theoretical dependence, Eq. (1). Upper left inset: schematic illustration of the interlayer e-h friction in SA TBG at finite D. Lower right inset: Prefactor $\mathcal{B}$ as a function of twist angle, θ.

increasing T for both D values, indicating characteristic behavior of doped graphene sheets. On the contrary, at the NP, ρ_{xx} exhibits a very different behavior for the two cases. Namely, at $D = 0$, ρ_{xx} drops rapidly when T is raised from 4.2 to 40 K [inset of Fig. 3(a)], whereas at $D = 0.7$ V/nm, ρ_{xx} shows a clear metallic trend: the resistivity increases with increasing T [inset of Fig. 3(b)].

It is now instructive to normalize all measured $\rho_{xx}(T)$ dependencies to their lowest T value in order to compare the functional forms of the T dependencies in different cases. At $T = 40$ K, the zero-D resistivity of the SA TBG device is less than a half of its 4.2 K value; further increase of T leads to a very slow ascending trend of $\rho_{xx}(T)$. At the same T and $D = 0.7$ V/nm, ρ_{xx} experiences a more than 2 times increase and keeps growing with increasing T following approximately an $a + bT^2$ dependence, where a and b are constants [dashed black line in the inset of Fig. 3(b)]. To compare, we have also measured the resistivity of a BLG device of comparable quality as a function of n and T [Fig. 3(c)]. At the NP, ρ_{xx} is practically unaffected by the T variation [Fig. 3(c)] over the entire range of T in our experiments.

The above observations clearly point to the difference in the conductivity mechanisms of these three bilayer systems at their NPs. The weak insulating behavior of charge-neutral SA TBG at zero D resembles that of MLG: the resistivity drops as a result of the thermal activation of electrons and holes [8]. A further increase of T leads to the enhanced scattering between electron and hole nondegenerate subsystems hosted by SA TBG leading to an increase of the resistivity. In contrast, the flat T dependence of the BLG has been recently attributed to the perfect balance between the amount of thermally activated e-h pairs facilitating conductivity, and the e-h scattering that impedes the electrical current [22,26,47]. The peculiar T^2 growth of the resistivity in compensated SA TBG at finite D has not been observed previously. Below we show that this effect stems from the e-h friction [48,49] in this degenerate ambipolar system.

To demonstrate this, we solve the steady-state Boltzmann equation for e-h hole mixture in SA TBG; the details are given in Supplemental Material [41]. In the limit of temperatures much smaller than T_F, the resistivity due to e-h scattering reads as

$$\rho_{\mathrm{D}} \simeq \frac{8\pi\alpha_{\mathrm{ee}}^2 g(\bar{q}_{\mathrm{TF}})}{3ne^2 v_F^2 \hbar} (k_B T)^2. \tag{1}$$

where n is the particle density in each minivalley, $g(\bar{q}_{\mathrm{TF}}) = 3(\bar{q}_{\mathrm{TF}} - 1) + (4 - 3\bar{q}_{\mathrm{TF}}^2)\mathrm{arccoth}(1 + \bar{q}_{\mathrm{TF}})$, and $\bar{q}_{\mathrm{TF}} = N_f \alpha_{\mathrm{ee}}$ is the Thomas-Fermi screening wave vector in units of the Fermi wave vector. Here, $\alpha_{\mathrm{ee}} = e^2/[2\pi\epsilon_0(\epsilon_r + 1)\hbar v_F]$ is the effective fine-structure constant of Dirac fermions, ϵ_r is a dielectric constant accounting for screening due to far bands and external dielectrics, N_f is the number of flavors, and $\hbar$ is the reduced Planck constant. Hereafter we set $\epsilon_r = 3.9$, as for graphene deposited on h-BN. The total resistivity is then $\rho = \rho_0 + \rho_{\mathrm{D}}$, where ρ_0 is the zero-temperature resistivity due to momentum-nonconserving scattering processes. We also note that, as the minivalleys are predominantly formed from the energy bands of different graphene sheets, electrons and holes reside in the upper or lower graphene layers depending on the D direction [3,30,31], and thus ρ_{D} can be interpreted as the resistivity due to the interlayer e-h friction (see Supplemental Material [41]).

In Fig. 3(d) we compare the results of our calculations with $\rho_{xx}(T)$ found experimentally. To this end, we plot the experimentally found resistivity excess, $\Delta\rho = \rho_{xx}(T) - \rho_{xx}(4.2\ \mathrm{K})$, and theoretically obtained $\rho_{\mathrm{D}}(T)$. For the latter, we used an electrostatic model that accounts for screening effects to calculate the Fermi energy in each minivalley [30], as well as the experimentally determined twist angle. Using that, for $\theta = 1.65°$, $v_F \simeq 5 \times 10^5$ m/s (as determined from the continuum model of SA TBG [28,34,35]), for $D = 0.7$ V/m we estimate the carrier density $n = 1.3 \times 10^{15}$ m^{-2}. Experimental data closely follow the expected $\mathcal{B}T^2$ dependence with $\mathcal{B} \simeq 0.062\ \Omega/\mathrm{K}^2$ with some tendency to subquadratic dependence at higher T [inset of Fig. 3(b)].

Next, we analyze $\rho_{\mathrm{D}}(T)$ dependencies expected for other θ. We find that, at fixed carrier density, the resistivity due to e-h scattering depends on θ only through its dependence on the electron Fermi velocity v_F. In the inset of Fig. 3 we plot the ratio $\mathcal{B}(v_F)/\mathcal{B}(v_F^g)$ for a carrier density $n = 4 \times 10^{14}$ m^{-2} as a function of θ. Here, v_F^g is the Fermi velocity of MLG, while $\mathcal{B}(v_F)$ is defined from $\rho_{\mathrm{D}} = \mathcal{B}(v_F)T^2$. At $\theta > 3°$ the e-h drag would result in a 10 times smaller prefactor of the T^2 resistivity.

It would be instructive to put our observations in the context of electron transport in semimetals. Depending on the material, seemingly alike semimetallic e-h systems can display very different physical properties. For example, in charge-neutral MLG, frequent collisions between thermally activated electrons and holes impede electrical currents while leaving thermal ones untouched, causing a breakdown of the Wiedeman-Franz law. In this system the Lorentz ratio, i.e., the ratio between the thermal conductivity and its electrical counterpart, is found to be greatly enhanced [8]. On the contrary, in degenerate compensated semimetals such as WP_2 or Sb the Lorentz ratio has been found to be suppressed [50]. Despite their semimetallic nature, which would imply violations of the Wiedeman-Franz law akin to those observed in graphene [51], the behavior of these materials closely resembles that of conventional unipolar systems [52], where carriers of a single type transport both charge and heat. All these seemingly contradictory observations have stimulated a debate over the effect of quasiparticle statistics, band structure, and many-body interactions on the thermal and

electrical properties of these charge-neutral material platforms [51,53,54]. A definitive resolution of these long-lasting puzzles is made especially difficult by the fact that completely different behaviors are observed in different systems and regimes, and therefore a thorough comparison between them becomes challenging. The behavior of SA TBG observed in this Letter thus makes it a highly tunable platform for the exploration of different semimetallic regimes on an equal footing, allowing for a gradual transition between them. It would be interesting to further explore transport and thermal properties of *e*-*h* FLs in other polarizable layered systems with heavier charge carriers such as twisted double bilayer graphene [3] or twisted transition metal dichalcogenides [6] as well as to probe collective modes in such *e*-*h* mixtures [55–57].

The supporting data for Figs. 2 and 3 are openly available from [58].

The other data that support the findings of this study are available from the corresponding authors upon reasonable request. This work was supported by AFOSR Grant No. FA9550-21-1-0319 and the Gordon and Betty Moore Foundation's EPiQS Initiative through Grant No. GBMF9463 to P. J.-H. I. Y. P. acknowledges support from the MIT undergraduate research opportunities program and the Johnson and Johnson research scholars program. K. W. and T. T. acknowledge support from JSPS KAKENHI (Grants No. 19H05790, No. 20H00354, and No. 21H05233). A. P. acknowledges support from the European Commission under the EU Horizon 2020 MSCA-RISE-2019 program (Project No. 873028 HYDROTRONICS) and from the Leverhulme Trust under the Grant No. RPG-2019-363. The authors thank Clement Collignon, Alexey Berdyugin, and Dmitry Svintsov for productive discussions. D. A. B. and A. P. conceived and designed the study. D. A. B. and I. Y. P. fabricated and measured the devices. T. T. and K. W. grew high-quality *h*-BN crystals. A. P. developed the theory. P. J. H. supervised the project.

The authors declare no competing interests.

*Corresponding author.
dab@nus.edu.sg
†Corresponding author.
alepr85@gmail.com
‡Corresponding author.
pjarillo@mit.edu

[1] J. P. Eisenstein and A. H. MacDonald, Nature (London) **432**, 691 (2004).
[2] A. Perali, D. Neilson, and A. R. Hamilton, Phys. Rev. Lett. **110**, 146803 (2013).
[3] P. Rickhaus, F. K. de Vries, J. Zhu, E. Portoles, G. Zheng, M. Masseroni, A. Kurzmann, T. Taniguchi, K. Watanabe, A. H. MacDonald, T. Ihn, and K. Ensslin, Science **373**, 1257 (2021).
[4] M. Zarenia, D. Neilson, and F. M. Peeters, Sci. Rep. **7**, 11510 (2017).
[5] Y. Jia *et al.*, Nat. Phys. **18**, 87 (2022).
[6] Z. Zhang, E. C. Regan, D. Wang, W. Zhao, S. Wang, M. Sayyad, K. Yumigeta, K. Watanabe, T. Taniguchi, S. Tongay, M. Crommie, A. Zettl, M. P. Zaletel, and F. Wang, Nat. Phys. **18**, 1214 (2022).
[7] S. Rakhmanov, Zh. Eksp. Teor. Fiz. **75**, 160 (1978).
[8] J. Crossno, J. K. Shi, K. Wang, X. Liu, A. Harzheim, A. Lucas, S. Sachdev, P. Kim, T. Taniguchi, K. Watanabe, T. A. Ohki, and K. C. Fong, Science **351**, 1058 (2016).
[9] R. V. Gorbachev, A. K. Geim, M. I. Katsnelson, K. S. Novoselov, T. Tudorovskiy, I. V. Grigorieva, A. H. MacDonald, S. V. Morozov, K. Watanabe, T. Taniguchi, and L. A. Ponomarenko, Nat. Phys. **8**, 896 (2012).
[10] J. I. A. Li, T. Taniguchi, K. Watanabe, J. Hone, A. Levchenko, and C. R. Dean, Phys. Rev. Lett. **117**, 046802 (2016).
[11] J. C. W. Song, D. A. Abanin, and L. S. Levitov, Nano Lett. **13**, 3631 (2013).
[12] M. Titov, R. V. Gorbachev, B. N. Narozhny, T. Tudorovskiy, M. Schütt, P. M. Ostrovsky, I. V. Gornyi, A. D. Mirlin, M. I. Katsnelson, K. S. Novoselov, A. K. Geim, and L. A. Ponomarenko, Phys. Rev. Lett. **111**, 166601 (2013).
[13] M. Schütt, P. M. Ostrovsky, M. Titov, I. V. Gornyi, B. N. Narozhny, and A. D. Mirlin, Phys. Rev. Lett. **110**, 026601 (2013).
[14] J. C. W. Song and L. S. Levitov, Phys. Rev. Lett. **111**, 126601 (2013).
[15] L. Fritz, J. Schmalian, M. Müller, and S. Sachdev, Phys. Rev. B **78**, 085416 (2008).
[16] M. Müller, J. Schmalian, and L. Fritz, Phys. Rev. Lett. **103**, 025301 (2009).
[17] P. Gallagher, C.-S. Yang, T. Lyu, F. Tian, R. Kou, H. Zhang, K. Watanabe, T. Taniguchi, and F. Wang, Science **364**, 158 (2019).
[18] A. Block, A. Principi, N. C. H. Hesp, A. W. Cummings, M. Liebel, K. Watanabe, T. Taniguchi, S. Roche, F. H. L. Koppens, N. F. van Hulst, and K.-J. Tielrooij, Nat. Nanotechnol. **16**, 1195 (2021).
[19] A. Lucas and K. C. Fong, J. Phys. Condens. Matter **30**, 053001 (2018).
[20] D. Svintsov, V. Vyurkov, S. Yurchenko, T. Otsuji, and V. Ryzhii, J. Appl. Phys. **111**, 083715 (2012).
[21] B. N. Narozhny, I. V. Gornyi, M. Titov, M. Schütt, and A. D. Mirlin, Phys. Rev. B **91**, 035414 (2015).
[22] D. Y. H. Ho, I. Yudhistira, N. Chakraborty, and S. Adam, Phys. Rev. B **97**, 121404(R) (2018).
[23] C. Cao, E. Elliott, J. Joseph, H. Wu, J. Petricka, T. Schäfer, and J. E. Thomas, Science **331**, 58 (2011).
[24] E. Shuryak, Prog. Part. Nucl. Phys. **53**, 273 (2004), heavy Ion Reaction from Nuclear to Quark Matter.
[25] Y. Nam, D.-K. Ki, D. Soler-Delgado, and A. F. Morpurgo, Nat. Phys. **13**, 1207 (2017).
[26] C. Tan, D. Y. H. Ho, L. Wang, J. I. A. Li, I. Yudhistira, D. A. Rhodes, T. Taniguchi, K. Watanabe, K. Shepard, P. L. McEuen, C. R. Dean, S. Adam, and J. Hone, Sci. Adv. **8**, eabi8481 (2022).
[27] A. I. Berdyugin *et al.*, Science **375**, 430 (2022).
[28] R. Bistritzer and A. H. MacDonald, Proc. Natl. Acad. Sci. U.S.A. **108**, 12233 (2011).

[29] J. D. Sanchez-Yamagishi, T. Taychatanapat, K. Watanabe, T. Taniguchi, A. Yacoby, and P. Jarillo-Herrero, Phys. Rev. Lett. **108**, 076601 (2012).
[30] S. Slizovskiy, A. Garcia-Ruiz, A. I. Berdyugin, N. Xin, T. Taniguchi, K. Watanabe, A. K. Geim, N. D. Drummond, and V. I. Fal'ko, Nano Lett. **21**, 6678 (2021).
[31] F. K. de Vries, J. Zhu, E. Portolés, G. Zheng, M. Masseroni, A. Kurzmann, T. Taniguchi, K. Watanabe, A. H. MacDonald, K. Ensslin, T. Ihn, and P. Rickhaus, Phys. Rev. Lett. **125**, 176801 (2020).
[32] A. I. Berdyugin, B. Tsim, P. Kumaravadivel, S. G. Xu, A. Ceferino, A. Knothe, R. K. Kumar, T. Taniguchi, K. Watanabe, A. K. Geim, I. V. Grigorieva, and V. I. Fal'ko, Sci. Adv. **6**, eaay7838 (2020).
[33] I. Y. Phinney, D. A. Bandurin, C. Collignon, I. A. Dmitriev, T. Taniguchi, K. Watanabe, and P. Jarillo-Herrero, Phys. Rev. Lett. **127**, 056802 (2021).
[34] S. Fang, S. Carr, Z. Zhu, D. Massatt, and E. Kaxiras, arXiv:1908.00058.
[35] S. Carr, S. Fang, Z. Zhu, and E. Kaxiras, Phys. Rev. Res. **1**, 013001 (2019).
[36] K. Kim, M. Yankowitz, B. Fallahazad, S. Kang, H. C. P. Movva, S. Huang, S. Larentis, C. M. Corbet, T. Taniguchi, K. Watanabe, S. K. Banerjee, B. J. LeRoy, and E. Tutuc, Nano Lett. **16**, 1989 (2016).
[37] K. Kim, A. DaSilva, S. Huang, B. Fallahazad, S. Larentis, T. Taniguchi, K. Watanabe, B. J. LeRoy, A. H. MacDonald, and E. Tutuc, Proc. Natl. Acad. Sci. U.S.A. **114**, 3364 (2017).
[38] Y. Cao, J. Y. Luo, V. Fatemi, S. Fang, J. D. Sanchez-Yamagishi, K. Watanabe, T. Taniguchi, E. Kaxiras, and P. Jarillo-Herrero, Phys. Rev. Lett. **117**, 116804 (2016).
[39] J. M. Park, Y. Cao, K. Watanabe, T. Taniguchi, and P. Jarillo-Herrero, Nature (London) **592**, 43 (2021).
[40] D. G. Purdie, N. M. Pugno, T. Taniguchi, K. Watanabe, A. C. Ferrari, and A. Lombardo, Nat. Commun. **9**, 5387 (2018).
[41] See Supplemental Material at http://link.aps.org/supplemental/10.1103/PhysRevLett.129.206802 for device fabrication details, signatures of ballistic transport, and theoretical calculations of the interaction-dominated resistivity in SA-TBG.
[42] Z. Wang *et al.*, Sci. Adv. **5**, eaay8897 (2019).
[43] Y. Kim, P. Herlinger, P. Moon, M. Koshino, T. Taniguchi, K. Watanabe, and J. H. Smet, Nano Lett. **16**, 5053 (2016).
[44] A. A. Zibrov, E. M. Spanton, H. Zhou, C. Kometter, T. Taniguchi, K. Watanabe, and A. F. Young, Nat. Phys. **14**, 930 (2018).
[45] C. W. J. Beenakker and H. van Houten, Phys. Rev. Lett. **63**, 1857 (1989).
[46] A. S. Mayorov, R. V. Gorbachev, S. V. Morozov, L. Britnell, R. Jalil, L. A. Ponomarenko, P. Blake, K. S. Novoselov, K. Watanabe, T. Taniguchi, and A. K. Geim, Nano Lett. **11**, 2396 (2011).
[47] G. Wagner, D. X. Nguyen, and S. H. Simon, Phys. Rev. Lett. **124**, 026601 (2020).
[48] Z. D. Kvon, E. B. Olshanetsky, D. A. Kozlov, E. Novik, N. N. Mikhailov, and S. A. Dvoretsky, Low Temp. Phys. **37**, 202 (2011).
[49] V. L. Müller, Y. Yan, O. Kashuba, B. Trauzettel, M. Abdelghany, J. Kleinlein, W. Beugeling, H. Buhmann, and L. W. Molenkamp, Nano Lett. **21**, 5195 (2021).
[50] J. Gooth, F. Menges, N. Kumar, V. Süß, C. Shekhar, Y. Sun, U. Drechsler, R. Zierold, C. Felser, and B. Gotsmann, Nat. Commun. **9**, 4093 (2018).
[51] M. Zarenia, A. Principi, and G. Vignale, Phys. Rev. B **102**, 214304 (2020).
[52] A. Principi and G. Vignale, Phys. Rev. Lett. **115**, 056603 (2015).
[53] S. Li and D. L. Maslov, Phys. Rev. B **98**, 245134 (2018).
[54] P. S. Alekseev, A. P. Dmitriev, I. V. Gornyi, V. Y. Kachorovskii, B. N. Narozhny, M. Schütt, and M. Titov, Phys. Rev. Lett. **114**, 156601 (2015).
[55] V. Andreeva, D. A. Bandurin, M. Luskin, and D. Margetis, Phys. Rev. B **102**, 205411 (2020).
[56] A. Principi, D. Bandurin, H. Rostami, and M. Polini, Phys. Rev. B **99**, 075410 (2019).
[57] Z. Sun, D. N. Basov, and M. M. Fogler, Proc. Natl. Acad. Sci. U.S.A. **115**, 3285 (2018).
[58] 10.5281/zenodo.7256407.